Review Vol. 16, No. 11 / 1 Nov 2025 / *Biomedical Optics Express* 4333

Biomedical Optics EXPRESS

On the physiological processes underlying optoretinography [Invited]

HUAKUN LI,[1,†] YUEMING ZHUO,[2,†] VIMAL PRABHU PANDIYAN,[3,4] MOHAMMAD ASIF ZAMAN,[2] TONG LING,[1,5] RAMKUMAR SABESAN,[3,4] AND DANIEL PALANKER[2,6,*]

[1] *School of Chemistry, Chemical Engineering and Biotechnology, Nanyang Technological University, Singapore, Singapore*
[2] *Hansen Experimental Physics Laboratory, Stanford University, Stanford, CA, USA*
[3] *Department of Ophthalmology, University of Washington, Seattle, WA 98109, USA*
[4] *Roger and Angie Karalis Johnson Retina Center, Seattle, WA, USA*
[5] *SERI-NTU Advanced Ocular Engineering (STANCE) Program, Singapore, Singapore*
[6] *Department of Ophthalmology, Stanford University, Stanford, CA, USA*
[†] These authors contributed equally
[*] *palanker@stanford.edu*

Abstract: Optoretinography (ORG) is a label-free imaging of the light-evoked changes in the retina associated with alterations in the cell shape and refractive indices. Its most precise version, the phase-resolved optical coherence tomography (pOCT), exhibited sensitivity of about 10 nm *in vivo*, limited by the signal-to-noise ratio and accuracy of the tissue registration. While it is yet insufficient for the detection of single action potentials, which are about 1 nm in amplitude, it enables monitoring slower and larger deformations in other retinal layers. In response to a single flash delivered to the dark-adapted retina, photoreceptor outer segments (OS) exhibit rapid (millisecond-scale) contraction, reaching tens of nm in cones and hundreds of nm in rods. This effect can be explained by changes in the membrane tension due to hyperpolarization of the OS discs–that is, the intradiscal space becoming more negatively charged–during the early receptor potential induced by opsins isomerization. In cones, such contraction is followed by a slower elongation by hundreds of nm during hundreds of ms. The proposed underlying mechanisms include osmotic influx of water, swelling of the cone opsin and disc membranes, and conformational changes in phosphodiesterase (PDE6) during phototransduction. ORG also reveals slow deformations in the subretinal space (SRS) and retinal pigment epithelium (RPE), likely induced by light-evoked ionic and osmotic shifts, as well as in the inner plexiform layer (IPL) and ganglion cell layer (GCL). ORG has a high potential as a non-invasive, label-free, and objective assay of retinal health, co-registered with structural images in the same OCT machine. To realize its promise in basic science and clinical assessment of diseases and therapies, its underlying mechanisms need to be delineated. This review summarizes current understanding of the physiological mechanisms behind the ORG.

1. Introduction

Optical imaging technologies have revolutionized retinal diagnostics by enabling non-invasive visualization of the tissue structure and function [1]. Fundus photography [2,3], scanning laser ophthalmoscopy [4–6] and optical coherence tomography (OCT) [7–9] are widely used in clinics to assess retinal morphology and vasculature. OCT, in particular, offers depth-resolved imaging of retinal layers with micron-level resolution, making it indispensable in diagnosis and monitoring of ocular diseases, like age-related macular degeneration (AMD), diabetic retinopathy (DR), glaucoma and many others [10]. However, by the time morphological abnormalities are detected in the clinic, retinal cells may have already undergone irreversible functional impairment.

#573038 https://doi.org/10.1364/BOE.573038
Journal © 2025 Received 9 Jul 2025; revised 5 Sep 2025; accepted 23 Sep 2025; published 8 Oct 2025

Furthermore, incipient therapies for blinding diseases are limited by the lack of a safe, sensitive and non-invasive biomarker that can be used as an outcome measure in a short time-frame to test efficacy [11]. Together, these gaps highlight the need for functional imaging - detecting the stimulus-evoked physiological activity in retinal cells - that may not only reveal earlier signs of retinal diseases but also accelerate new treatments towards effective clinical translation.

Intrinsic optical signal (IOS) broadly refers to stimulus-evoked changes in the optical properties of tissues or cells, such as scattering, absorption and reflectance. These changes are typically related to neural activity, manifesting as alterations in the shape or refractive index of cells and tissues, as well as hemodynamic responses [12–17]. For example, it has been demonstrated that cells deform by about a nanometer during the action potential, attributed to voltage-dependent changes in the membrane tension [18,19]. These deformations were observed in cell cultures using quantitative phase imaging (QPI), capable of detecting the optical path length (OPL) changes with picometer sensitivity at sub-millisecond temporal resolution. The observed optical phase shifts related to the cell membrane displacements were tightly synchronized with electrical spikes, confirming that they reflect the changes in membrane potential.

IOS imaging in the retina, known today as optoretinography (ORG), can be performed using a variety of optical systems [20], including near-infrared microscopy [21], fundus cameras [14,17,22], or confocal ophthalmoscopes [23–25]. A particularly powerful implementation is the OCT-based physiological imaging [15,16,26–30]. In frequency-domain OCT (FD-OCT), the depth-resolved profile of the tissue scattering is computed by Fourier transform (FT) of the spectral interferogram arising from interference between the backscattered light from the sample and a reference beam (see Fig. 1). More specifically, the electric fields returning from the sample and the reference mirror, denoted by E_s and E_r, respectively, can be written as [31]

$$E_s = \frac{E_{in}}{\sqrt{2}} \sum_i r_{si} \exp(j2kz_{si}), \tag{1}$$

$$E_r = \frac{E_{in}}{\sqrt{2}} r_r \exp(j2kz_r), \tag{2}$$

where $E_{in} = s(k)\exp[j(kz - \omega t)]$ is the polychromatic plane wave incident on the 50/50 beam splitter; k and ω denote the wavenumber and angular frequency. $s(k)$ represents the electric field amplitude as a function of the wavenumber, j is the imaginary unit, z and t denote the OPL and time, respectively. r_r and z_r are the electric field reflectivity and OPL of the reference mirror. For simplicity, the sample is modeled as a series of discrete layers, where r_{si} and z_{si} represent reflectivity and OPL of the i^{th} layer.

The signal detected in the spectrometer, denoted as $I(k)$, is proportional to the squared amplitude of $E_s + E_r$,

$$\begin{aligned} I(k) &\propto |E_s + E_r|^2 = |E_r|^2 + |E_s|^2 + E_s E_r^{*} + c.c. \\ &= \frac{S(k)}{2}\left(r_r^2 + \sum_i r_{si}^2\right) \text{ “DC terms”} \\ &+ \frac{S(k)}{2} \sum_{i \neq l} r_{si} r_{sl} \exp[j2k(z_{si} - z_{sl})] \text{ “Auto-correlation terms”} \\ &+ \frac{S(k)}{2} \sum_i r_r r_{si} \exp[j2k(z_{si} - z_r)] + c.c. \text{ “Cross-correlation terms”} \end{aligned} \tag{3}$$

where $S(k) = s(k)^2$ is the power spectral density of the light source, $*$ represents complex conjugate, and $c.c.$ denotes the complex conjugate term.

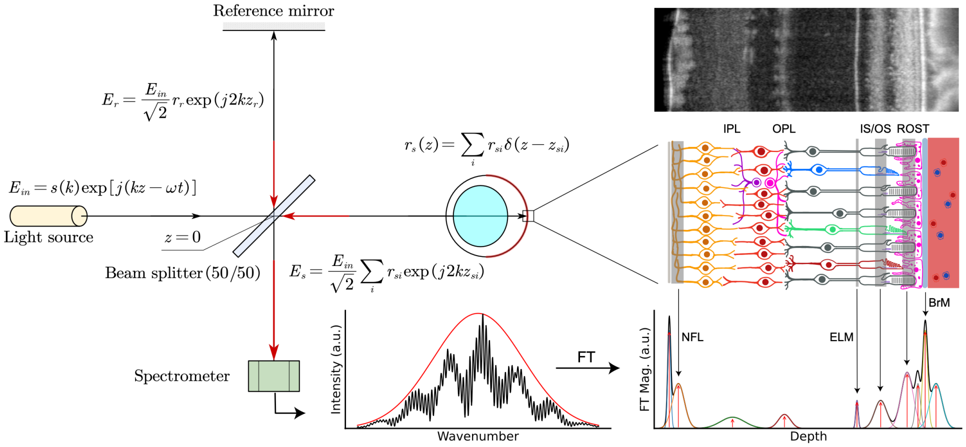

Fig. 1. Schematic of a spectral-domain OCT system based on a Michelson interferometer. The spectral interferogram, resulting from the interference between backscattered light from the retina and a reference beam, is captured by a spectrometer. A Fourier transform (FT) is then applied to reconstruct the depth-resolved scattering. NFL: nerve fiber layer; IPL: inner plexiform layer; OPL: outer plexiform layer; ELM: external limiting membrane; IS/OS: inner segment/outer segment junction; ROST: rod outer segment tip; BrM: Bruch's membrane.

Taking the FT of the first cross-correlation term in Eq. (3), and assuming that the light source has a Gaussian-shaped spectrum with a bandwidth (standard deviation) of Δk, the resulting complex-valued OCT signal consists of a sum of phasor contributions [31]:

$$i_{\mathrm{OCT}}(z) = \frac{r_r}{2}\sum_i r_{si}\exp[-\Delta k^2(z-(z_{si}-z_r))^2]\exp[-j2k_c(z-(z_{si}-z_r))], \tag{4}$$

where k_c is the central wavenumber of the light source. The product of two exponential terms, a real-valued Gaussian envelope and a complex oscillatory phase term, arises from the complex-valued coherence function. The Gaussian envelope determines the axial resolution of the OCT system: $\delta z = \frac{2\ln 2}{\pi}\cdot\frac{\lambda_c^2}{\Delta\lambda_{\mathrm{FWHM}}}$ [31], where λ_c and $\Delta\lambda_{\mathrm{FWHM}}$ denote the central wavelength and the full width at half maximum (FWHM) of the light source. Accordingly, the axial resolution of typical near-infrared OCT systems (λ_c = 840 nm, $\Delta\lambda_{\mathrm{FWHM}}$ ranging from 30 nm to 100 nm) is approximately 3-10 µm in air, with broader bandwidth yielding finer axial resolution.

The complex oscillatory phase term in Eq. (4) enables phase-based measurements with nanometer-scale sensitivity [32]. To elucidate the principle, we consider a moving sample in the sample arm. For simplicity, the sample is modeled as a single-layer reflector with reflectivity of r_s, and its position, expressed in OPL, is $z_s(t)$. According to Eq. (4), the complex-valued OCT signal detected at the position $z_s(0) - z_r$ can be expressed as,

$$i_{\mathrm{OCT}}(z_s(0)-z_r) = \frac{r_r r_s}{2}\exp(-\Delta k^2\Delta z_s^2(t))\exp(j2k_c\Delta z_s(t)), \tag{5}$$

where $\Delta z_s(t) = z_s(t) - z_s(0)$ is the displacement of the sample. The phase component of the OCT signal is $2k_c\Delta z_s(t)$, which directly encodes the sample movement.

Several pipelines of signal analysis are employed in the OCT-based ORG technique:

- Monitoring the changes in the scattering intensity of retinal layers following visual stimulation [15,16,26–28,33], such as increased reflectivity in the photoreceptor outer segments (OS) and decreased reflectivity in the inner segments (IS) in response to white light stimulation observed in isolated rabbit retinae [16]. Both changes were synchronized with electroretinography (ERG), confirming that these optical responses were tied to physiological processes.

- Measuring morphological alterations in hyper-reflective retinal bands. In this approach, deconvolution techniques or multimodal Gaussian fitting are applied to averaged OCT A-lines to extract quantitative parameters, such as the axial position, amplitude and FWHM of each hyper-reflective band [30,34]. As in super-resolution microscopy, localization accuracy of the centroid of an object can exceed the resolution limit of the system's instantaneous point-spread function (PSF) [35]. For example, it has been shown that following a flash bleaching 10% of rhodopsin in rod photoreceptors of mouse retina, the backscattering from the inner segment/outer segment junction (IS/OS) significantly increased, and it moved ~2 µm farther from the Bruch's membrane (BrM) [30]. These responses were absent in mice lacking the rod transducin (G-protein alpha-subunit $G\alpha_t$), indicating that the increase in light scattering and movement of that retinal band were associated with phototransduction.
- In phase-resolved OCT, calculating the phase difference between two layers along an A-line cancels out common OPL fluctuations, leaving only the relative OPL change of interest with nm-scale sensitivity [29,36]. Accordingly, phase-based ORG revealed light-induced deformations of the photoreceptor OS [29,37–45], the subretinal space (SRS) [46,47] and the inner plexiform layer (IPL) [48].

Although the intensity-based method can detect the retinal bands movement at sub-micron level, surpassing the system's axial PSF [30], phase-based measurements can provide about a tenfold improvement in motion detection sensitivity [47]. Fundamentally, sensitivity of the phase-resolved OCT is limited by the signal-to-noise ratio (SNR). When SNR $\gg$ 1, the SNR-dependent phase stability can be calculated as [32,49]

$$\sigma_{\mathrm{SNR}} = \sqrt{\frac{1}{\mathrm{SNR}}} \tag{6}$$

in radians, where SNR is determined by both the system's sensitivity and by reflectivity of the measured sample. Empirically, the SNR can be estimated by dividing the mean squared magnitude of the OCT signal–i.e., the OCT intensity–at a specific retinal layer by the variance of the background noise measured in a signal-free region. Retinal reflections in OCT vary by approximately 2.5 orders of magnitude, ranging from -60 dB (10^{-6} in cone OS and RPE) to -85 dB ($10^{-8.5}$ in outer nuclear layer) [50]. With a typical OCT system sensitivity of 95 dB, it yields an SNR of 35 dB at cone OS and corresponding phase stability of 0.02 rad or 1.2 nm (with a central wavelength of 840 nm).

Phase stability *in vivo* is further affected by the decorrelation noise arising from variations in speckle patterns within the probed region [51,52]. These variations can result from bulk sample movement, pulsatile deformations, and the diffusion of scatterers related to cellular activity. Among these factors, bulk tissue movement is the primary source of noise when detecting ORG signals in the outer retina. Statistically, in fully developed speckle patterns, the phase variation ϕ induced by the bulk sample movement follows the distribution [53]

$$p(\phi) = \frac{1-\alpha^2}{2\pi(1-\alpha^2\cos^2\phi)}\left[1 + \frac{\alpha\cos\phi}{\sqrt{1-\alpha^2\cos^2\phi}}(\pi - \cos^{-1}(\alpha\cos\phi))\right], \tag{7}$$

$$\alpha = \exp\left(-\frac{\Delta x^2 + \Delta y^2}{{w_0}^2}\right)\cdot\exp\left(-\frac{\Delta z^2}{2{l_c}^2}\right), \tag{8}$$

where the parameter α evaluates the correlation magnitude between the speckle patterns, l_c represents the coherence length, and w_0 denotes the waist radius of the OCT beam on the sample.

Δx, Δy and Δz are bulk movements along the fast-scan, slow-scan, and axial directions. The standard deviation of decorrelation noise can be calculated by

$$\sigma_{\text{decor}} = \sqrt{\int_{-\pi}^{\pi} p(\phi)\phi^2 d\phi}, \tag{9}$$

The total phase noise can be computed as

$$\sigma_{tot} = \sqrt{\sigma_{\text{SNR}}^2 + \sigma_{\text{decor}}^2}. \tag{10}$$

According to Eqs. (7) and (8), the decorrelation noise caused by bulk sample movement can be effectively mitigated by registering repeated scans with subpixel precision [54]. For an OCT system with a central wavelength of 840 nm, a coherence length of 2 µm, a spot radius of 6 µm, and assuming residual bulk movements (after subpixel-level registration) ($\Delta x', \Delta y', \Delta z'$) to be (0.1 µm, 2 µm, 0.1 µm) ($\Delta y'$ is much larger since the slow out-of-plane axis has sparser sampling points than the fast axis), we obtain $\alpha = 0.89$, yielding $\sigma_{\text{decor}} = 47$ nm (see Supplement 1 Fig. 1). This is much larger than 1.2 nm σ_{SNR} calculated above for SNR = 35 dB, indicating that the decorrelation noise is the dominant noise source in phase-based ORG measurements *in vivo*. Meanwhile, spatially averaging across independent speckle patterns reduces both the decorrelation noise and SNR-dependent noise at the cost of spatial resolution. Nevertheless, it is still very challenging to achieve sensitivity below 1 nm while maintaining sufficient spatiotemporal resolution to detect single action potentials [18,19].

Using phase-resolved OCT, Hillmann et al. observed biphasic OPL changes in the cone OS spatially matching the light stimulus pattern – fast initial decrease by a few nm, followed by a slower increase up to hundreds of nanometers, lasting for hundreds of ms [29]. Following publications provided additional details about the light-induced retinal deformations [37,39,40,44–46,48], described their applications to cone classification [38,55] and disease diagnostics [41,56], and suggested the underlying mechanisms [30,39,42–45]. This review focuses on cellular mechanisms that give rise to ORG signals, with a particular emphasis on rod and cone OS dynamics during phototransduction.

2. ORG of photoreceptor outer segments

Rod and cone photoreceptors enable vision across a wide range of illumination intensities. Rods are specialized for dim light, capable of detecting even single photons, while cones mediate vision in daylight and enable color vision [57]. Differences in their sensitivity are partly attributed to variations in transduction proteins, resulting in faster activation and slower inactivation of phototransduction in rod outer segments compared to cones [58]. Other factors facilitating the exceptional sensitivity of rods under dim light conditions include (1) lower intrinsic noise, (2) high quantum efficiency of photoisomerization, and (3) high photon capture efficiency enabled by densely stacked disc membranes [57].

Rod outer segments differ significantly in shape and disc organization compared to cones [59]. Specifically, rod OS has a long cylindrical structure composed of hundreds of discrete and enclosed discs stacked in parallel, separated from the plasma membrane (Fig. 2). In contrast, cone OSs are shorter tapering structures, in which the disc membranes are direct infoldings of the common plasma membrane.

Upon photon absorption, visual pigments undergo a sequence of isomerization intermediates before reaching the biochemically active metarhodopsin II (Meta II), a process accompanied by charge transfer across the membrane [60,61]. Patch-clamp electrical recordings *ex vivo* revealed a rapid biphasic early receptor potential (ERP) in both cone and rod photoreceptors: a brief depolarizing phase (R1), followed by a dominant hyperpolarizing phase (R2) [62–64]. For example, in turtle red cones, the R1 phase peaks at ~2 mV around 1 ms, and the R2 phase

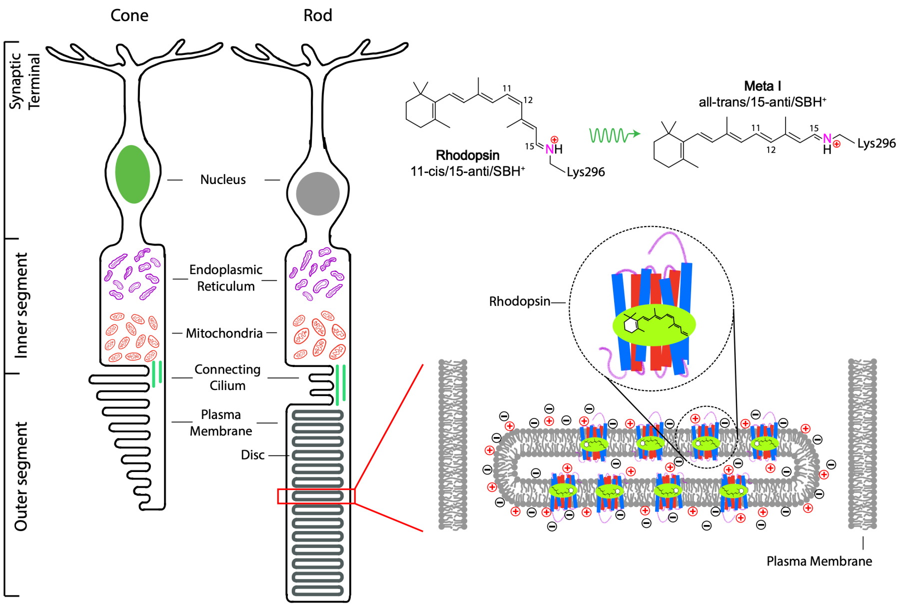

Fig. 2. Diagram of the rod and cone photoreceptor cell compartments, with emphasis on rhodopsin molecules embedded in the disc membranes of the outer segment. Light detection begins by photoisomerization of 11-cis retinal to all-trans retinal, which changes the opsin structure to enable the signal amplification in phototransduction.

reaches a peak of ~7 mV at around 7 ms (Supplement 1 Fig. 2) [63]. The brief R1 phase of ERP corresponds to the formation of metarhodopsin I (Meta I), while the subsequent R2 phase reflects the transition from Meta I to Meta II [63]. In living human eyes, the ERP signal originates primarily from cone photoreceptors [65], since the charge movement across the closed rod disc membranes lacks a conductive path to extracellular space, making the transmembrane voltage changes across the rod OS discs undetectable by electrodes [66]. Some ERP signals may still be detectable in rods due to few newly forming discs that remain as evaginations not yet separated from the plasma membrane, and from rhodopsin molecules embedded in the plasma membrane [67].

Release of osmolytes into cytoplasm during phototransduction induces osmotic imbalance within the photoreceptor OS, leading to water influx (see Section 4.1). The resulting swelling can vary substantially between rods and cones due to their morphological differences: in cone OS, the infoldings of the plasma membrane have greater effective permeability allowing for easier and faster expansion in response to water influx than in rod OS, where discs are enclosed within a tight cylindrical membrane.

Phase-based ORG typically measures the phase difference between the IS/OS and the OS tip (OST), denoted as ϕ_{OS}, to obtain light-evoked deformations of photoreceptor OS (see Fig. 3):

$$\Delta \mathrm{OPL} = \frac{\lambda_c}{4\pi} \cdot (\phi_{\mathrm{OS}} - \phi_{\mathrm{OS}}^{\mathrm{pre}}), \tag{11}$$

where $\phi_{\mathrm{OS}} = \phi_{\mathrm{OST}} - \phi_{\mathrm{IS/OS}}$, $\phi_{\mathrm{OS}}^{\mathrm{pre}}$ represents such a phase difference before the visual stimulus, λ_c is the central wavelength of the OCT system.

Using phase-sensitive measurements, several groups have detected rapid contractile responses to strong stimuli in human cone OS, followed by a slower elongation with a much larger amplitude [29,38,39], as shown in Fig. 3(A). In rodent rod OS, the maximum contraction amplitude is significantly larger than that in cones (>200 nm vs. ~50 nm), while elongation is much smaller

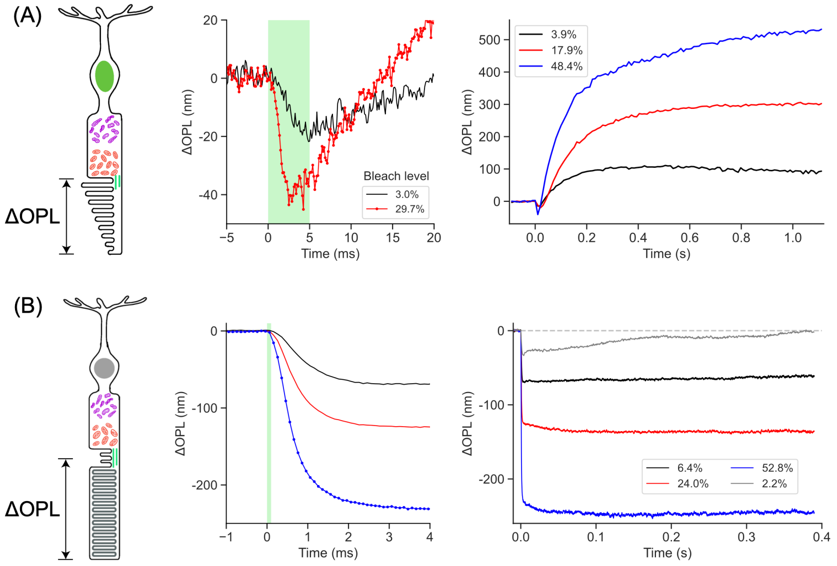

Fig. 3. Photoreceptor outer segment (OS) dynamics evoked by strong stimuli. (A) ΔOPL in human cone OS elicited by 5-ms flashes (528 nm) at various bleach levels (adapted from Pandiyan et al., 2020 [39], licensed under CC BY 4.0). Temporal resolution of traces in the middle column: 0.125 ms. (B) ΔOPL in the rat rod OS in response to 0.1-ms stimuli (520 nm) at various bleach levels (adapted from Zhuo et al., 2025 [45]). Temporal resolution: 0.1 ms.

and observed only at low bleach levels (Fig. 3(B)) [44,45]. Amplitude of the contractile response increases with the bleach level and recovery becomes slower [45]: at 2.2% bleach, return to baseline takes about 400 ms, while at 6.4% and beyond, no recovery is seen within the 400-ms measurement window (Fig. 3(B)). Longer recordings showed that the contracted state persists for tens of seconds at bleach levels >12% [44].

Given that the rapid OS contraction aligns with the millisecond timescale of Meta II formation [60,68], it has been hypothesized that this response is associated with the photoisomerization of the visual pigments [29,38]. In addition, a few observations provide insights into the underlying mechanisms of this rapid response: (1) the contraction amplitude increases logarithmically with increasing bleach level [39,44,45]; (2) the latency of the contraction decreases with stronger stimuli [39,45].

3. Mechanisms of rapid contraction of the outer segments

3.1. Voltage-dependent membrane tension model

The rapid contraction can be explained by a voltage-dependent membrane tension model associated with the ERP [69]. Briefly, the shape of biological cells is determined by a balance between the intracellular hydrostatic pressure, membrane tension, and strain imposed by the cytoskeleton [70]. Membrane tension consists of the lipid bilayer tension and lateral electrostatic repulsion of mobile ions within the Debye layer. During the R2 phase of ERP, membrane hyperpolarization increases the electrostatic repulsion among ions in Debye layer, leading to lateral expansion of the disc membranes [69]. Due to volume conservation during this millisecond-scale process, the lateral stretch is accompanied by axial contraction of each disc, resulting in an overall shortening of the photoreceptor OS.

In cones, the late elongation of OS due to phototransduction truncates the initial contraction and impedes observing the latter's entire time-course (see Section 4). Therefore, we use the experimental results from rodent rod OS to elucidate the time-dependence of the electromechanical model. The change in the transmembrane voltage associated with the charge transfer during Meta II isomerization can be calculated by [45]

$$\Delta V_m(t) = m_2(t) \cdot \frac{\sigma_{\text{rho}} \cdot q}{c_m}, \tag{12}$$

where $m_2(t)$ denotes the relative concentration of Meta II molecules, which is normalized to the concentration of rhodopsin in the dark state. σ_{rho} is the area density of rhodopsin molecules in disc membranes, c_m is the specific membrane capacitance, and $q = 0.14e^-$ is the charge shift per photoisomerization [44]. The resulting increase in repulsive force on the membrane surface is linearly proportional to the change in transmembrane voltage, of about 0.1 mN/m per V, or 10 μN/m for a 100 mV hyperpolarization [19,69].

If the increased repulsive force is balanced by a restoring force that increases exponentially with the membrane expansion [69], such a quasistatic model can adequately describe the contraction amplitude as a function of the bleach level (blue curves in Fig. 4(C)). However, the dynamics of the contraction predicted by this quasistatic model is much faster than the experimental result (compare black and blue curves in Fig. 4(C)), suggesting the involvement of viscous effects.

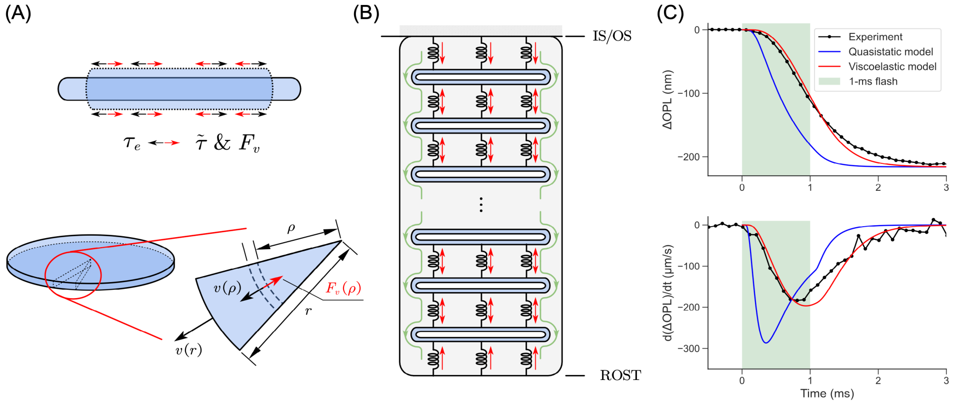

Fig. 4. Rod outer segment (OS) viscoelastic modeling (adapted from Zhuo et al., 2025 [45]). (A) Top: Axial contraction of a single disc due to lateral expansion under increased repulsive force and conservation of the disc volume. Bottom: Geometry of the radially expanding disc, with the lateral friction force pointing radially inward. (B) Rod OS with distributed spacers connecting the discs. Red arrows show the direction of axial stretching of the spacers due to axial contraction of discs. Green arrows indicate the flow of cytoplasm relative to the axially moving discs. IS/OS: inner segment/outer segment junction; ROST: rod outer segment tip. (C) Measured ΔOPL responses to a 1-ms flash and predictions of the quasistatic model and the viscoelastic model. Bottom plot represents a time derivative of the data from the top plot, corresponding to the contraction rate.

Since the contraction of rod OS arises from the cumulative contraction of individual discs connected by spacers, two viscous effects that dampen this process are considered. First, illustrated in Fig. 4(A), is a shear-induced friction from the surrounding medium at the top and bottom surfaces of each disc during lateral expansion, which is linearly proportional to the local velocity through a damping coefficient [69]. Second, shown in Fig. 4(B), are the axial frictional forces acting on the disc side walls when OS contracts [45]. These viscous interactions resist the rapid deformation and contribute to the observed delay, as illustrated by red lines in Fig. 4(C).

The dramatically different membrane time constants between rod and cone disc membranes may contribute to the much slower expansion rate in rod OS following the rapid contraction. In patch-clamp recordings, the rising phase of ERP originates from light-induced charge transfer across the membrane, while the falling phase reflects resistive discharge through the plasma membrane (Supplement 1 Fig. 2) [63]. Since cone discs are confluent with the plasma membrane, the passive discharge rate is determined by the plasma membrane time constant, which typically ranges from several ms to a few tens of ms [63,64]. In contrast, rod disc membranes are isolated from the plasma membrane and exhibit exceptionally high specific membrane resistance (on the order of $M\Omega \cdot cm^2$) due to the lack of ion channels [71,72]. Given a typical specific membrane capacitance of $1\ \mu F \cdot cm^{-2}$ [64], this results in a membrane time constant on the order of seconds. The much longer membrane time constant in rod discs allows sustained hyperpolarizing ERP and the associated electromechanical contraction to persist for a prolonged time.

Another unique signature observed in rodent rod OS is a secondary contraction – peaking between 5 and 15 s – in response to stimuli with bleach levels exceeding 15% [44]. Previous studies have suggested that a substantial reduction in photoreceptor dark current may lead to an osmolarity-driven shrinkage of the rod OS [73,74].

In contrast to rodents, human rods exhibit substantially faster kinetics of OS shrinkage [44]. Human rods show a larger amplitude of OS shrinkage than cones (maximum contraction: ~100 nm vs. ~50 nm) but do not sustain the prolonged contraction as rodents. In rodents, ~97% photoreceptors are rods [57], so cones are unlikely to have a noticeable impact on the measured rod ORG signals. However, in the human retina, rod OS responses could be influenced by the movement of surrounding cones, especially given the large amplitude and relatively fast elongation of cone OS following a stimulus.

We cannot exclude some alternative mechanisms driving the rapid contraction that could be associated with mechanical changes in rhodopsin upon isomerization into the active Meta II state, including the 7 Å shift of helix 6 and other smaller changes of its shape upon opening of a binding site for transducin [75,76]. Like with an electrostatic stretch described above, such lateral expansion of the discs will lead to their axial contraction due to conservation of volume during ms-short events. Currently, however, there isn't any quantitative description along these lines.

3.2. Reversible isomerization upon UV stimulation

Previous electrophysiological recordings of photoreceptors demonstrated that a brief 400-nm flash delivered to Meta II can evoke an electrical response with positive polarity - opposite to that of the ERP (Supplement 1 Fig. 3) [61,77]. ORG response associated with this process has been measured by delivering a UV flash (1 ms, 385 nm) following a strong bleaching of rhodopsin by a 1-ms green flash (520 nm). At pulse energy of 340 µJ, green flash bleached nearly all rhodopsin, as confirmed by the minimal residual response to a second green flash delivered 200 ms later (Fig. 5(A)).

A UV flash (at 100 ms) following that bleaching green flash induced an opposite ΔOPL (Fig. 5(B)) - elongation of the rod OS, which confirms that polarity of the mechanical response corresponds to polarity of the changes in membrane potential, as expected from the electromechanical coupling process. The second green flash (at 200 ms), following the UV one, elicited a rapid contraction with an amplitude greater than that observed in the control experiment, suggesting that UV light regenerated photosensitive molecules capable of inducing this rapid contraction. The second UV flash again produced rod OS elongation, demonstrating repeatability of these responses. Amplitude of the elongation following the first UV flash exhibits a saturating trend with increasing UV pulse energy [45].

As shown in Fig. 6, UV light can induce 15-anti to 15-syn isomerization in Meta II, leading to the reverted-Meta (R-Meta) state, which decays thermally to the metarhodopsin III (Meta III) state via protonation at the Schiff base. Notably, the thermal relaxation from Meta I to Meta

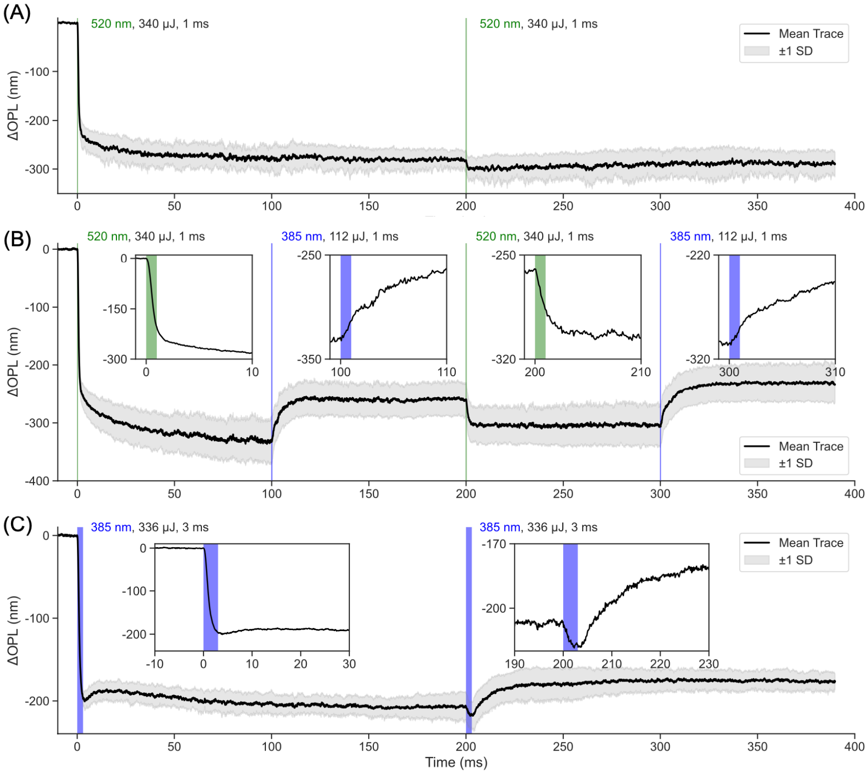

Fig. 5. Reversible isomerization with green and UV stimulation (adapted from Zhuo et al., 2025 [45]). (A) Control experiment: ORG responses to two green flashes (1 ms, 340 μJ measured in front of the cornea, corresponding to 3.6×10^8 photons/μm^2 on the retina) delivered 200 ms apart. (B) Response to a flash sequence of green-UV-green-UV. The energy of each 1-ms UV flash was 112 μJ measured in front of the cornea, corresponding to 7.5×10^7 photons/μm^2 incident on the retina and a bleach level of 22%. Insets show the first 10-ms time window. (C) ORG responses to two UV pulses (3 ms, 336 μJ, 52% bleach level, 200-ms apart). Insets show the first 30-ms time window. Gray bands represent the standard deviation (SD) range.

II involves Schiff base deprotonation and is associated with rapid contraction. Therefore, the reverse process—protonation during the R-Meta to Meta III transition—is likely responsible for the observed elongation. When Meta III absorbs a green photon, it can undergo 15-syn to 15-anti isomerization to regenerate Meta I, followed by the Schiff base deprotonation, thereby completing the activation cycle.

Remarkably, when a UV flash was applied directly to the dark-adapted retina, it evoked the characteristic rapid contraction observed previously with green flashes, followed by a much slower and weaker elongation (Fig. 5(C)). This result suggests that UV photons can also initiate the transition from rhodopsin to Meta II. Indeed, the rhodopsin absorption at 385 nm is approximately 0.2 of its peak in the green range [78]. Consequently, prior to the second UV flash, the rod OS contains a mixture of rhodopsin, Meta II and a small fraction of Meta III. Upon the second UV flash, three photochemical pathways will be activated simultaneously: (1) rhodopsin transitions through Meta I to Meta II, (2) Meta II progresses to Meta III, and (3) Meta III reverts to Meta II via Meta I. The first and third pathways are associated with rod OS contraction, while the

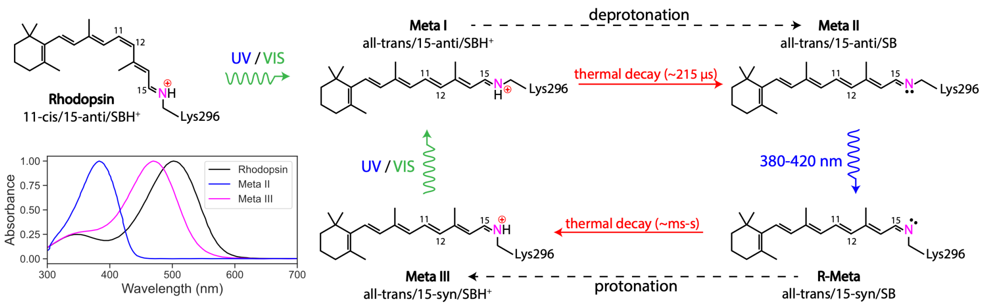

Fig. 6. Photo-intermediates and their transitions under green and UV light. The inset shows the absorption spectra of bovine rhodopsin, Meta II and Meta III, each normalized to its respective peak absorption (adapted from Sakai et al., 2022 [78], licensed under CC BY 4.0). SB: Schiff base; SBH$^+$: protonated Schiff base.

second pathway induces elongation [45]. The morphological response of the rod OS observed in Fig. 5(C) arises from the combined effects of these competing processes.

4. Slow expansion of the outer segments

Following a rapid, millisecond-scale contraction immediately upon exposure to light (Comp0), the cone OS elongates for hundreds of ms reaching an amplitude of up to hundreds of nanometers (Fig. 7(A)) [29,38,42,79]. The elongation trace (black curve in Fig. 7(A)) can be accurately modeled as the sum of two distinct exponential components (red and blue curves in Fig. 7(A)), with time constants differing by more than an order of magnitude. For various stimulus intensities, each trace in the response family can be fit as a weighted sum of the same pair of exponential functions (Fig. 7(B)). Across all tested light levels, with bleach levels ranging from 0.9% to 73.9%, the distinct components differ by 13-fold in maximum rate, 3 to 6-fold in light sensitivity, and over 50-fold in small-signal gain [42]. The distinct time constants of the two elongation components suggest that they arise from fundamentally different biochemical processes. Following elongation, the cone OS gradually returns to baseline, with stronger bleaches exhibiting slower recovery [29,37,79]. The kinetics and light sensitivity of this recovery process remains an area of ongoing investigation.

Cones show markedly different kinetics, sensitivity, and amplitude of the OS elongation, compared to rods [40]. This discrepancy is partly attributed to their distinct membranous organizations (see Fig. 3). Moreover, structural and kinetic differences in downstream processes of phototransduction likely explain the differing amplitudes, rates, and saturation behaviors of rod and cone swelling [58].

4.1. Changes in the shape of outer segments due to osmotic pressure

Studies of isolated frog rod photoreceptor demonstrated that outer segments change their length, width and volume in response to light [80]. Similar shape changes were observed with varying the concentration of surrounding media, indicating the role of osmotic pressure [80]. These shape changes were thought to be the basis of variations in light scattering and retinal layer thickness upon visual stimulation in mice [30].

Osmotic imbalance caused by osmolytes produced during phototransduction (Figs. 8(A) and (B)) leads to water entry into the OS, resulting in its elongation [30,42]. In rods, downstream of Gα_t (the alpha subunit of transducin) activation is likely to contribute to the increased osmotic pressure [30]. At high light intensities, the G-protein complex in rods dissociates, detaches from

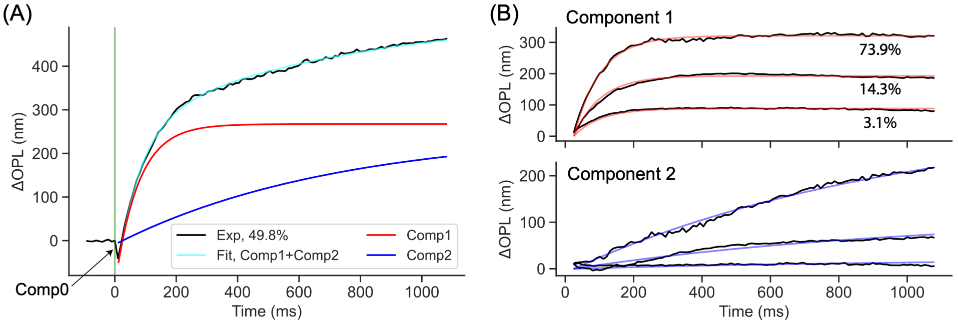

Fig. 7. Decomposition of the cone ORG response into distinct temporal components (adapted from Pandiyan et al., 2022 [42]). (A) The experimental ΔOPL trace (black) exhibits an initial rapid decrease immediately post-stimulus (Comp0), followed by a slow increase. The latter is modeled as the sum (cyan) of two rising exponential functions, representing Comp1 (red) and Comp2 (blue), corresponding to temporally distinct phases of the optical response. (B) Both components increase in amplitude and rate with increasing light intensity.

the disc membrane, and translocates within the OS [81], disrupting osmotic equilibrium and promoting water influx.

The rapid onset and high light sensitivity of Comp1 in cones suggest that it arises from an osmotic response to an amplified soluble by-product of phototransduction [42]. Several mechanisms, including G-protein subunit dissociation, metabolites of cGMP hydrolysis, and by-products of guanylate cyclase activity, were evaluated and rejected due to inconsistencies in their kinetics and amplification. The evidence instead pointed to phosphate (Pi) produced by RGS9-catalyzed hydrolysis of GTP within G-protein–PDE complexes as the most plausible source (Fig. 8(B)). This is further supported by the fact that cones express RGS9-1 at significantly higher levels than rods [82,83]. A phototransduction model incorporating this mechanism reproduced the light-dependence and time course of Comp1 and also aligned with human cone ERG responses [84]. This hypothesis could be tested in patients with bradyopsia, a visual disorder associated with mutations in RGS9 and related proteins [84–86].

4.2. *Other mechanisms underlying the slow OS elongation*

The amplitude of Comp2 in cones, on the other hand, demonstrates a linear dependence on the amount of bleached cone opsin [42]. Three mechanisms were proposed for Comp2: (1) a volume increase in cone opsin following chromophore isomerization [30,87], (2) swelling of disc membranes due to at-ROL (all-trans retinol) localization following chromophore hydrolysis and reduction by retinol dehydrogenase (RDH), and (3) release of at-ROL into the cytosol acting as an osmolyte [30]. The third hypothesis was ruled out due to the low solubility of retinol. The data most strongly support the combined effect of opsin swelling and membrane expansion due to water uptake following chromophore hydrolysis and the formation of membrane-associated at-ROL (Fig. 8(C)) [42]. This process is rate-limited by chromophore hydrolysis and proceeds with a time constant of approximately one second, matching the kinetics of Comp2. The hypothesis that Comp2 results from water influx into photoactivated opsins may be tested using advanced imaging techniques, such as combined OCT and two-photon retinol fluorescence microscopy [88,89].

Tomczewski et al. recently proposed that OS elongation may additionally be driven by conformational changes in PDE6 [43], which is considered the most plausible candidate for the pillar protein anchoring adjacent photoreceptor discs [90]. The light-induced conformational change in PDE6 extends the inter-disc space by 30 Å each, stacking such deformations across

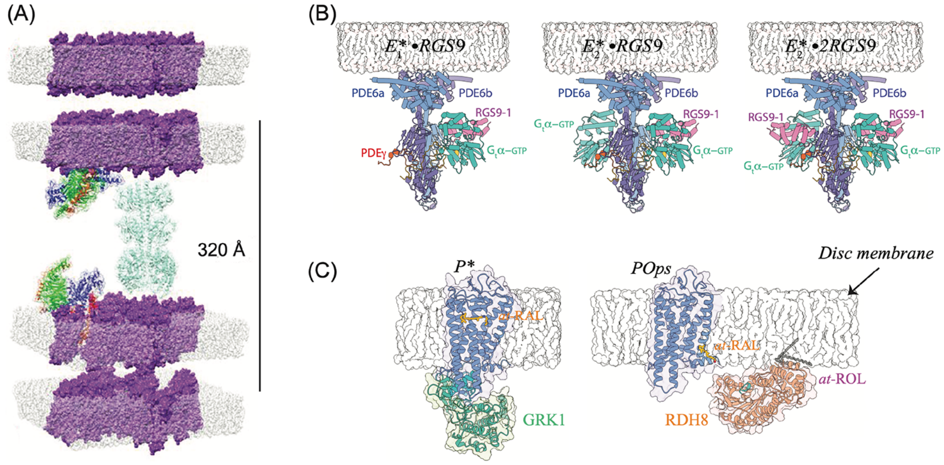

Fig. 8. Swelling mechanism of the outer segment. (A) Structural model (adapted from Zhang et al., 2017 [30]) of a 20 × 20 nm patch showing two pairs of adjacent disc bilayers in a dark-adapted rod, including rhodopsin molecules (magenta), G-protein complexes (Gα_t in blue, Gβ_1 in green, Gγ_1 in red), and PDE6 complex (cyan). Upon stimulation, the G-protein heterotrimers dissociate into Gα_t and G$\beta_1\gamma_1$ subunits and solubilize into the cytoplasm, increasing osmotic pressure and driving water into OS. (B) Molecular basis of Comp1 in cones (adapted from Pandiyan et al., 2022 [42]). Three PDE6 complexes—E_1^*•RGS9 (left), E_2^*•RGS9 (middle), and E_2^*•2RGS9 (right)-catalyze the hydrolysis of Gα_t–GTP via RGS9, releasing phosphate (Pi). Accumulation of Pi raises osmotic pressure, leading to water influx and contributing to Comp1 elongation. $E_1^* =$ PDE•Gα_t and $E_2^* =$ PDE•2Gα_t. (C) Molecular basis of Comp2 in cones (adapted from Pandiyan et al., 2022 [42]). (Left) At low light levels, photoactivated opsin (P*) is deactivated through phosphorylation by GRK1 followed by arrestin binding. (Right) Under high light conditions, this pathway saturates, and opsin deactivation proceeds via chromophore hydrolysis. RDH8 reduces all-trans retinal (at-RAL) to all-trans retinol (at-ROL) at the membrane–cytosol interface. This process induces water uptake, leading to swelling of both cone opsin and the disc membranes, which underlies Comp2 elongation.

multiple discs was suggested to lead to an overall increase in OS length by up to a few micrometers. Inhibiting PDE6 with Sildenafil significantly reduced the elongation of rod OS in dark-adapted mice [43]. This observation was attributed to both diminished PDE6 activation and the consequent reduction in downstream phototransduction cascade by-products that are responsible for the slow OS elongation.

4.3. Bidirectional changes in the outer segment length elicited by flickering stimulation

While most studies have investigated ORG signals in response to a single flash delivered after dark adaptation (2 hours to overnight for rodents [44,45,91]; a few minutes for human cone ORG experiments [29,38,39]; and 15–30 minutes for human rod ORG experiments [40,44]), several studies have also measured ORG responses under photopic conditions using flickering stimulation [92,93]. In humans, measurements in cones and rods revealed bidirectional changes in photoreceptor OS length synchronized with the modulation of the flickering stimulation, which has been hypothesized to be mediated by conformational changes in PDE6 [43].

5. Deformations in other retinal layers

5.1. Deformations in the subretinal space

In response to a 1-ms visual stimulus at a bleach level of 0.26%, distinct dynamics of different layers in the rodent outer retina have been separated using unsupervised machine learning (Figs. 9(A) and (B)) [46]. Note that the bleach level here is much smaller than the ones typically used to investigate the rod OS contractile response (>2%) [44,45]. According to the electromechanical coupling model (see Section 3), the rapid contraction amplitude at a bleach level of 0.26% is ∼3 nm, which is close to the noise floor and can easily be obscured by the late elongation. These factors likely account for the absence of a detectable contractile OS response in Fig. 9(B). Instead, the rod OS expands by tens of nanometers within ∼1 s, undergoes a negative undershoot, and returns to baseline within ∼15 s. Interestingly, unlike the swelling of the hyperpolarized OS, the hyperpolarized RPE [95] is getting compressed by approximately 20 nm at ∼3 s, followed by a gradual recovery. The SRS, on the other hand, exhibits a slower but larger expansion, with its rate reaching maximum of about 15 nm/s around 1.5 s after the stimulus, and maintained during the following 10 s, until it gradually decreases. The IS is compressed by about 10 nm during the first 1.5 s, after which it exhibits dynamics like the SRS, albeit with lower amplitude.

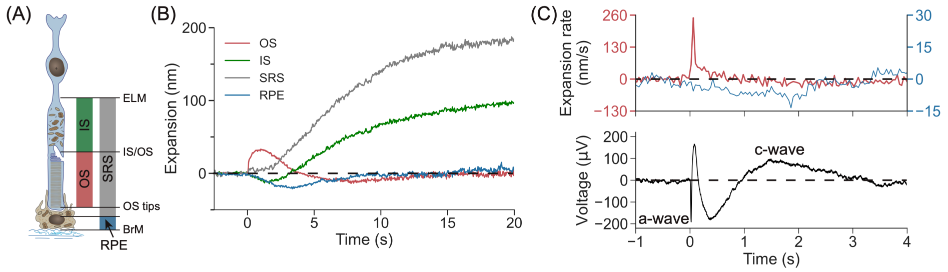

Fig. 9. Light-evoked deformations in subretinal space over time and comparison with electroretinography (ERG). Adapted from Tan et al., 2024 [46], licensed under CC BY 4.0. (A) Schematic of a rod photoreceptor and the underlying retinal pigment epithelium (RPE)–Bruch's membrane (BrM) complex. (B) Deformations of the rod outer segment (OS), inner segment (IS), RPE, and subretinal space (SRS) following a 1-ms visual stimulus at a 0.26% bleach level. (C) Expansion rates of the OS (red) and RPE (blue), derived from time derivatives of the traces in panel (B), shown together with a representative ERG trace in response to a white flash [94].

Figure 9(C) depicts the expansion rate (time derivative of deformation), which is likely related to the water flux, alongside the ERG trace. The photoreceptors' response to visual stimuli (a-wave in ERG) begins 10 ms after the stimulus, corresponding to the onset of the OS expansion in ORG. The c-wave in ERG, associated with a potassium current through RPE following the phototransduction cascade, peaks at about 1.5 s. Notably, the RPE contraction rate also reaches its maximum between 1 and 2 s after the stimulus, overlapping with the time course of the c-wave.

These ORG signatures may provide valuable insights into the physiology of the photoreceptor–RPE interaction and expand the diagnostic capabilities of ORG. The RPE plays a crucial role in mediating the flow of nutrients and metabolites, as well as maintaining ion homeostasis in the SRS [96,97]. Interruption of the photoreceptor dark current in response to visual stimuli results in a depletion of K^+ from the SRS to photoreceptors. Decreased K^+ concentration in SRS leads to (1) reduced or reversed electrochemical driving force of the apical membrane Na-K-Cl cotransporter, thereby reducing or reversing the attendant water flow from SRS into RPE [98]; (2) increase in the conductive efflux of K^+ across the RPE apical membrane, which hyperpolarizes the RPE. The hyperpolarized RPE enhances Cl^- efflux across the RPE basal membrane. The conductive effluxes of K^+ and Cl^- lead to osmolarity-driven shrinkage of the RPE and expansion of the SRS [98]. Additionally, NaHCO3 cotransport across apical membrane may also contribute to light-induced SRS hydration. Since NaHCO3 transport is electrogenic ($HCO3^-$:Na^+ = 1:3), RPE hyperpolarization reduces the rate of transepithelial $HCO3^-$ influx and the associated fluid flow [99].

5.2. Deformations in the inner retina

A few pilot studies in the living human retina using a full-field OCT reported a ~40 nm increase in the OPL between GCL and IPL during light stimulation [100,101]. In particular, OPL increased up to 30 nm by the end of the 8 seconds stimulation in the top strata of IPL, where ON cells are wired, and decreased by about 20 nm in the bottom strata, where OFF cells are wired [48,101]. A 10-Hz flicker dramatically increased a response in the central IPL, where reside the axon terminals of bipolar cells that respond more transiently [102]. These observations indicate activity of the inner retinal neurons and may provide insights into the retinal physiology and expand the diagnostic capabilities of ORG.

6. Outlook

Over the past 2 decades, the growth of ORG has been significantly propelled by multiple innovations in retinal imaging technology. These include faster swept sources for illumination, multiplexed detection, parallel recordings employing line-scan and full-field geometries, and utilization of adaptive optics (AO). These technologies have enabled high-speed optical recordings that effectively overcome retinal motion and helped visualize rapid light-evoked events within the retina *in vivo* at cellular resolution.

Notably, phase-resolved OCT technology holds promise to advance the discovery of retinal signals that remain imperceptible at the moment, particularly those originating in the inner retina. The fact that action potentials can be detected interferometrically *in vitro* as rapid cellular deformations on the order of 1 nm in 1 ms [19] is an encouraging indication that if a similar SNR can be replicated *in vivo*, it should allow imaging neural spiking in the retina. Stabilizing the ORG probe on a specific cell or a retinal layer of interest by tracking eye movements in real time is one important advancement in this direction [103,104]. Similarly, recent progress in eye-tracking and adaptive optics scanning laser ophthalmoscopy (AOSLO) have enabled precise stimulation of single and groups of photoreceptors in the living human retina [105]. In addition, improved post-processing algorithms [54,106,107] and new OCT acquisition protocols [93] have been developed to mitigate signal decorrelation, thereby enhancing the SNR of ORG signals and facilitating the clinical translation of ORG techniques.

Technological advancements enable higher quality ORG recordings, which provide additional insights to studies of the underlying physiological processes. As described in this review, these investigations have shed new light on the shape changes of retinal cells and their biochemical and physiological basis. Despite this progress, much remains to be uncovered. A key challenge—and opportunity—is to reconcile findings from classical literature, largely based on *in vitro* retinal preparations, with emerging *in vivo* observations made possible through ORG. One such example is the quantification of bleaching, for which representative calculation procedures are detailed on our recent studies [44,45]. As a light-intensity dependent phenomenon, the precise quantification of photoisomerization and bleaching forms the bedrock for the interpretation of all photoreceptor ORGs and eventually their translational applications. Pandiyan et al. [42] noted a 3-fold discrepancy between the photosensitivity of opsins measured *in situ* versus all other extant measures obtained *in vivo* using reflection densitometry and psychophysics [108–113]. Light capture by cones is affected by several factors that vary with eccentricity, including the Stiles-Crawford Effect [114], the inner segment diameter [115], the outer segment diameter and length. By accounting for the properties that govern light propagation in the cone, including the eccentricity-dependent changes in the waveguide condensation of light from the inner to the outer segment, this discrepancy was reconciled [42]. A similar treatment that unifies the quantification of bleach level across different subject groups will be needed to study the effect of aging and disease on the photoreceptor ORG. As a start, to unify measurements from different variants of the ORG, it is suggested that bleach strength be reported as photon density following the recipe outlined in Jiang et al. [116], which accounts for both the stimulus source properties, as well as subject-specific anatomical considerations (pupil size, axial length etc.) that together define the photons per unit area on the retinal surface and ultimately the level of photoisomerizations. To further understand the physiological mechanisms of the ORG, it will be essential to compare healthy individuals and wild-type animals with specific genetic mutations purported to have abnormalities in ORG. These comparisons will help generate testable hypotheses and refine the underlying theoretical framework for describing its mechanisms. *In vitro* recordings remain important for the development of protocols that can be reliably translated to *in vivo* applications and compared with established electrophysiological methods, including those incorporating pharmacological agents to block specific channels or pathways.

Regardless of the technology platform or the level of understanding of the underlying physiological mechanisms, ORG is already emerging as a valuable tool for clinical investigations [117]. Notably, ORG deficits have been detected even in retinal areas that appear structurally normal in cases of inherited retinal diseases [41,56,118–120]. In the first application of ORG in a longitudinal study [121], deterioration in COS function over time measured with ORG preceded deficits in retinal structure - ellipsoid zone width and outer segment length – by ~7 to 10-fold. By detecting functional impairment ahead of visible structural changes, ORG is positioned as an early biomarker of therapeutic efficacy for future clinical trials and has the potential to accelerate the life cycle of incipient therapies. Realizing this potential requires a comprehensive normative characterization of ORG across a healthy, diverse population, along with the development of standardized protocols—similar to the ISCEV standards established for ERG. Besides inherited retinal disease, ORG has been effective in rodent models in identifying subtle functional changes associated with Alzheimer's disease [122] and in tracking dark adaptation of rod photoreceptors [123]. These findings support its potential utility in detecting functional changes in the retina that accompany normal aging, various forms of retinal degeneration and other neurological diseases.

Funding. National Institutes of Health (U01 EY032055, EY029710); Air Force Office of Scientific Research (FA9550-20-1-0186); Research to Prevent Blindness; Dawn's Light Foundation; George and Martina Kren Professorship in Vision Research; National Research Foundation Singapore (NRF-NRFF14-2022-0005); Nanyang Technological University (the Startup Grant); National Medical Research Council (MOH-001748).

Acknowledgements. We thank Dr. Edward Pugh from UC Davis, Dr. Krzysztof Palczewski from UC Irvine and Dr. Wayne Hubbell from UCLA for fruitful discussions. This work was funded by the National Institutes of Health (U01 EY032055, EY029710), Air Force Office of Scientific Research (FA9550-20-1-0186), Research to Prevent Blindness, Dawn's Light Foundation, George and Martina Kren Professorship in Vision Research, the National Research Foundation, Singapore for the NRF Fellowship Award (NRF-NRFF14-2022-0005), the Startup Grant from Nanyang Technological University, and the National Medical Research Council, Singapore (MOH-001748).

Disclosures. The authors declare that there are no conflicts of interest related to this article.

Data availability. No data were generated or analyzed in the presented research.

Supplemental document. See Supplement 1 for supporting content.

References

1. A. Arrigo, E. Aragona, M. Battaglia Parodi, *et al.*, "Quantitative approaches in multimodal fundus imaging: State of the art and future perspectives," Prog. Retinal Eye Res. **92**, 101111 (2023).
2. V. Gulshan, L. Peng, M. Coram, *et al.*, "Development and Validation of a Deep Learning Algorithm for Detection of Diabetic Retinopathy in Retinal Fundus Photographs," JAMA **316**(22), 2402–2410 (2016).
3. F. Grassmann, J. Mengelkamp, C. Brandl, *et al.*, "A Deep Learning Algorithm for Prediction of Age-Related Eye Disease Study Severity Scale for Age-Related Macular Degeneration from Color Fundus Photography," Ophthalmology **125**(9), 1410–1420 (2018).

4. A. Roorda, F. Romero-Borja, W. J. Donnelly III, *et al.*, “Adaptive optics scanning laser ophthalmoscopy,” Opt. Express **10**(9), 405–412 (2002).
5. J. Fischer, T. Otto, F. Delori, *et al.*, “Scanning Laser Ophthalmoscopy (SLO),” in *High Resolution Imaging in Microscopy and Ophthalmology: New Frontiers in Biomedical Optics*, J.F. Bille, ed. 2019, Springer International Publishing: Cham. p. 35–57.
6. P. F. Sharp, A Manivannan, H Xu, *et al.*, “The scanning laser ophthalmoscope—a review of its role in bioscience and medicine,” Phys. Med. Biol. **49**(7), 1085–1096 (2004).
7. D. Huang, E. A. Swanson, C. P. Lin, *et al.*, “Optical coherence tomography,” Science **254**(5035), 1178 (1991).
8. W. Drexler and J. G. Fujimoto, “State-of-the-art retinal optical coherence tomography,” Prog. Retinal Eye Res. **27**(1), 45–88 (2008).
9. A. H. Kashani, C.-L. Chen, J. K. Gahm, *et al.*, “Optical coherence tomography angiography: A comprehensive review of current methods and clinical applications,” Prog. Retinal Eye Res. **60**, 66–100 (2017).
10. J.S. Schuman, J. G. Fujimoto, J. Duker, *et al.*, *Optical coherence tomography of ocular diseases*. 2024: CRC Press.
11. L. Schmetterer, H. Scholl, G. Garhöfer, *et al.*, “Endpoints for clinical trials in ophthalmology,” Prog. Retinal Eye Res. **97**, 101160 (2023).
12. A. Grinvald, E. Lieke, R. D. Frostig, *et al.*, “Functional architecture of cortex revealed by optical imaging of intrinsic signals,” Nature **324**(6095), 361–364 (1986).
13. R. A. Stepnoski, A LaPorta, F Raccuia-Behling, *et al.*, “Noninvasive detection of changes in membrane potential in cultured neurons by light scattering,” Proc. Natl. Acad. Sci. U. S. A. **88**(21), 9382 (1991).
14. K. Tsunoda, Y. Oguchi, G. Hanazono, *et al.*, “Mapping Cone- and Rod-Induced Retinal Responsiveness in Macaque Retina by Optical Imaging,” Invest. Ophthalmol. Visual Sci. **45**(10), 3820–3826 (2004).
15. X.-C. Yao, A. Yamauchi, B. Perry, *et al.*, “Rapid optical coherence tomography and recording functional scattering changes from activated frog retina,” Appl. Opt. **44**(11), 2019–2023 (2005).
16. K. Bizheva, R. Pflug, B. Hermann, *et al.*, “Optophysiology: Depth-resolved probing of retinal physiology with functional ultrahigh-resolution optical coherence tomography,” Proc. Natl. Acad. Sci. **103**(13), 5066–5071 (2006).
17. R. S. Jonnal, J. Rha, Y. Zhang, *et al.*, “In vivo functional imaging of human cone photoreceptors,” Opt. Express **15**(24), 16141–16160 (2007).
18. T. Ling, K. C. Boyle, G. Goetz, *et al.*, “Full-field interferometric imaging of propagating action potentials,” *Light: Sci. Appl.* 7(1), 107 (2018).
19. T. Ling, K. C. Boyle, V. Zuckerman, *et al.*, “High-speed interferometric imaging reveals dynamics of neuronal deformation during the action potential,” Proc. Natl. Acad. Sci. **117**(19), 10278–10285 (2020).
20. X. Yao and B. Wang, “Intrinsic optical signal imaging of retinal physiology: a review,” J. Biomed. Opt. **20**(9), 090901 (2015).
21. X.-C. Yao and Y.-B. Zhao, “Optical dissection of stimulus-evoked retinal activation,” Opt. Express **16**(17), 12446–12459 (2008).
22. M. D. Abràmoff, Y. H. Kwon, D. Ts’o, *et al.*, “Visual Stimulus–Induced Changes in Human Near-Infrared Fundus Reflectance,” Invest. Ophthalmol. Visual Sci. **47**(2), 715–721 (2006).
23. K. Grieve and A. Roorda, “Intrinsic Signals from Human Cone Photoreceptors,” Invest. Ophthalmol. Visual Sci. **49**(2), 713–719 (2008).
24. R. F. Cooper, W. S. Tuten, A. Dubra, *et al.*, “Non-invasive assessment of human cone photoreceptor function,” Biomed. Opt. Express **8**(11), 5098–5112 (2017).
25. R. F. Cooper, D. H. Brainard, and J. I. W. Morgan, “Optoretinography of individual human cone photoreceptors,” Opt. Express **28**(26), 39326–39339 (2020).
26. V. J. Srinivasan, M. Wojtkowski, J. G. Fujimoto, *et al.*, “In vivo measurement of retinal physiology with high-speed ultrahigh-resolution optical coherence tomography,” Opt. Lett. **31**(15), 2308–2310 (2006).
27. V. J. Srinivasan, Y. Chen, J. S. Duker, *et al.*, “In Vivo Functional Imaging of Intrinsic Scattering Changes in the Human Retina with High-speed Ultrahigh Resolution OCT,” Opt. Express **17**(5), 3861–3877 (2009).
28. T. Schmoll, C. Kolbitsch, and R. Leitgeb, “In vivo functional retinal optical coherence tomography,” J. Biomed. Opt. **15**(4), 041513 (2010).
29. D. Hillmann, H. Spahr, C. Pfäffle, *et al.*, “In vivo optical imaging of physiological responses to photostimulation in human photoreceptors,” Proc. Natl. Acad. Sci. U. S. A. **113**(46), 13138–13143 (2016).
30. P. Zhang, R. Zawadzki, R. Goswami, *et al.*, “In vivo optophysiology reveals that G-protein activation triggers osmotic swelling and increased light scattering of rod photoreceptors,” Proc. Natl. Acad. Sci. U. S. A. **114**(14), E2937–E2946 (2017).
31. J.A. Izatt, M.A. Choma, and A.-H. Dhalla, “*Theory of Optical Coherence Tomography*,” *in Optical Coherence Tomography: Technology and Applications*, W. Drexler and J.G. Fujimoto, eds. 2015, Springer International Publishing: Cham. p. 65–94.
32. M. A. Choma, A. K. Ellerbee, C. Yang, *et al.*, “Spectral-domain phase microscopy,” Opt. Lett. **30**(10), 1162–1164 (2005).
33. G. Ma, T. Son, T.-H. Kim, *et al.*, “In vivo optoretinography of phototransduction activation and energy metabolism in retinal photoreceptors,” J. Biophotonics **14**(5), e202000462 (2021).
34. P. Zhang, S. J. Karlen, G. P. Allina, *et al.*, “Whole retina light-evoked optoretinography (ORG) under different retina hydration levels: modeling of Bruch’s membrane ORGs,” Biomed. Opt. Express **16**(5), 1944–1959 (2025).

35. L. Schermelleh, A. Ferrand, T. Huser, *et al.*, "Super-resolution microscopy demystified," Nat. Cell Biol. **21**(1), 72–84 (2019).
36. R. S. Jonnal, O. P. Kocaoglu, Q. Wang, *et al.*, "Phase-sensitive imaging of the outer retina using optical coherence tomography and adaptive optics," Biomed. Opt. Express **3**(1), 104–124 (2012).
37. M. Azimipour, J. V. Migacz, R. J. Zawadzki, *et al.*, "Functional retinal imaging using adaptive optics swept-source OCT at 1.6 MHz," Optica **6**(3), 300–303 (2019).
38. F. Zhang, K. Kurokawa, A. Lassoued, *et al.*, "Cone photoreceptor classification in the living human eye from photostimulation-induced phase dynamics," Proc. Natl. Acad. Sci. U. S. A. **116**(16), 7951–7956 (2019).
39. V. P. Pandiyan, A. Maloney-Bertelli, J. A. Kuchenbecker, *et al.*, "The optoretinogram reveals the primary steps of phototransduction in the living human eye," Sci. Adv. **6**(37), eabc1124 (2020).
40. M. Azimipour, D. Valente, K. V. Vienola, *et al.*, "Optoretinogram: optical measurement of human cone and rod photoreceptor responses to light," Opt. Lett. **45**(17), 4658–4661 (2020).
41. A. Lassoued, F. Zhang, K. Kurokawa, *et al.*, "Cone photoreceptor dysfunction in retinitis pigmentosa revealed by optoretinography," Proc. Natl. Acad. Sci. **118**(47), e2107444118 (2021).
42. V. P. Pandiyan, P. T. Nguyen, E. N. Pugh, *et al.*, "Human cone elongation responses can be explained by photoactivated cone opsin and membrane swelling and osmotic response to phosphate produced by RGS9-catalyzed GTPase," Proc. Natl. Acad. Sci. **119**(39), e2202485119 (2022).
43. S. Tomczewski, A. Curatolo, A. Foik, *et al.*, "Photopic flicker optoretinography captures the light-driven length modulation of photoreceptors during phototransduction," Proc. Natl. Acad. Sci. **122**(7), e2421722122 (2025).
44. H. Li, C. W. Weiss, V. P. Pandiyan, *et al.*, "Optoretinography reveals rapid rod photoreceptor movement upon photoisomerization," bioRxiv (2025).
45. Y. Zhuo, H. Li, M. Bhuckory, *et al.*, "Label-free Imaging of the Reversible Rhodopsin Dynamics in a Living Eye," bioRxiv (2025), Accepted for publication in Nature Communications.
46. B. Tan, H. Li, Y. Zhuo, *et al.*, "Light-evoked deformations in rod photoreceptors, pigment epithelium and subretinal space revealed by prolonged and multilayered optoretinography," Nat. Commun. **15**(1), 5156 (2024).
47. E. Pijewska, P. Zhang, M. Meina, *et al.*, "Extraction of phase-based optoretinograms (ORG) from serial B-scans acquired over tens of seconds by mouse retinal raster scanning OCT system," Biomed. Opt. Express **12**(12), 7849 (2021).
48. C. Pfäffle, H. Spahr, K. Gercke, *et al.*, "Phase-Sensitive Measurements of Depth-Dependent Signal Transduction in the Inner Plexiform Layer," Front. Med. **9**, 885187 (2022).
49. J.W. Goodman, *Statistical Optics*. 2015: John Wiley & Sons.
50. D. T. Miller and K. Kurokawa, "Cellular-Scale Imaging of Transparent Retinal Structures and Processes Using Adaptive Optics Optical Coherence Tomography," Annu. Rev. Vis. Sci. **6**(1), 115–148 (2020).
51. B. Hyle Park, B. Pierce, M. C. Cense, *et al.*, "Real-time fiber-based multi-functional spectral-domain optical coherence tomography at 1.3 µm," Opt. Express **13**(11), 3931–3944 (2005).
52. B. J. Vakoc, G. J. Tearney, and B. E. Bouma, "Statistical properties of phase-decorrelation in phase-resolved Doppler optical coherence tomography," IEEE Trans. Med. Imaging **28**(6), 814 (2009).
53. M.G.O. Grafe, O. Nadiarnykh, and J.F. De Boer, "Optical coherence tomography velocimetry based on decorrelation estimation of phasor pair ratios (DEPPAIR)," Biomed. Opt. Express **10**(11), 5470–5485 (2019).
54. H. Li, B. Tan, V. P. Pandiyan, *et al.*, "Phase-restoring subpixel image registration: enhancing motion detection performance in Fourier-domain optical coherence tomography," J. Phys. D: Appl. Phys. **58**(14), 145102 (2025).
55. V. P. Pandiyan, S. Schleufer, E. Slezak, *et al.*, "Characterizing cone spectral classification by optoretinography," Biomed. Opt. Express **13**(12), 6574–6594 (2022).
56. B. J. Wendel, V. P. Pandiyan, T. Liu, *et al.*, "Multimodal High-Resolution Imaging in Retinitis Pigmentosa: A Comparison Between Optoretinography, Cone Density, and Visual Sensitivity," Invest. Ophthalmol. Visual Sci. **65**(10), 45 (2024).
57. Y. Fu and K.-W. Yau, "Phototransduction in mouse rods and cones," Pflugers Arch. - Eur. J. Physiol. **454**(5), 805–819 (2007).
58. N. T. Ingram, A. P. Sampath, and G. L. Fain, "Why are rods more sensitive than cones?" The Journal of Physiology **594**(19), 5415–5426 (2016).
59. D. Mustafi, A. H. Engel, and K. Palczewski, "Structure of cone photoreceptors," Prog. Retinal Eye Res. **28**(4), 289–302 (2009).
60. K. P. Hofmann and T. D. Lamb, "Rhodopsin, light-sensor of vision," Prog. Retinal Eye Res. **93**, 101116 (2023).
61. R. A. Cone and W. H. Cobbs, "Rhodopsin Cycle in the Living Eye of the Rat," Nature **221**(5183), 820–822 (1969).
62. M. Murakami and W. L. Pak, "Intracellularly recorded early receptor potential of the vertebrate photoreceptors," Vision Res. **10**(10), 965–975 (1970).
63. A. L. Hodgkin and P. M. Obryan, "Internal recording of the early receptor potential in turtle cones," The Journal of Physiology **267**(3), 737–766 (1977).
64. C. L. Makino, W. R. Taylor, and D. A. Baylor, "Rapid charge movements and photosensitivity of visual pigments in salamander rods and cones," The Journal of Physiology **442**(1), 761–780 (1991).
65. E. B. Goldstein and E. L. Berson, "Cone Dominance of the Human Early Receptor Potential," Nature **222**(5200), 1272–1273 (1969).

66. R. A. Cone, G. M. Curry, M. E. Feinleib, *et al.*, The early receptor potential. principles of receptor physiology, 1971: p. 345–365.
67. C. Kessler, M. Tillman, M. E. Burns, *et al.*, "Rhodopsin in the rod surface membrane regenerates more rapidly than bulk rhodopsin in the disc membranes in vivo," The Journal of Physiology **592**(13), 2785–2797 (2014).
68. R. R. Birge, "Nature of the primary photochemical events in rhodopsin and bacteriorhodopsin," Biochim. Biophys. Acta, Bioenerg. **1016**(3), 293–327 (1990).
69. K. C. Boyle, Z.C. Chen, T. Ling, *et al.*, "Mechanisms of Light-Induced Deformations in Photoreceptors," Biophys J **119**(8), 1481–1488 (2020).
70. A. Diz-Muñoz, D. A. Fletcher, and O. D. Weiner, "Use the force: membrane tension as an organizer of cell shape and motility," Trends Cell Biol. **23**(2), 47–53 (2013).
71. R. Uhl, P. V. Kuras, K. Anderson, *et al.*, "A light scattering study on the ion permeabilities of dark-adapted bovine rod outer segment disk membranes," Biochimica et Biophysica Acta (BBA) - Biomembranes **601**, 462–477 (1980).
72. T. I. Rebrik, G. R. Kalamkarov, and M. A. Ostrovskiĭ, "The absence of channel structures in the photoreceptor membrane of the rod disc," Biofizika **31**(6), 985 (1986).
73. M. Chabre and A. Cavaggioni, "Light Induced Changes of Ionic Flux in the Retinal Rod," Nat. New Biology **244**(134), 118–120 (1973).
74. N. Yagi, "Structural changes in rod outer segments of frog and mouse after illumination," Exp. Eye Res. **116**, 395–401 (2013).
75. J. H. Park, P. Scheerer, K. P. Hofmann, *et al.*, "Crystal structure of the ligand-free G-protein-coupled receptor opsin," Nature **454**(7201), 183–187 (2008).
76. H.-W. Choe, Y. J. Kim, J. H. Park, *et al.*, "Crystal structure of metarhodopsin II," Nature **471**(7340), 651–655 (2011).
77. R. A. Cone, "Early Receptor Potential: Photoreversible Charge Displacement in Rhodopsin," Science **155**(3766), 1128–1131 (1967).
78. K. Sakai, Y. Shichida, Y. Imamoto, *et al.*, "Creation of photocyclic vertebrate rhodopsin by single amino acid substitution," eLife **11**, e75979 (2022).
79. D. Valente, K. V. Vienola, R. J. Zawadzki, *et al.*, "Insight into human photoreceptor function: Modeling optoretinographic responses to diverse stimuli," Sci. Adv. **11**(24), eadq7332 (2025).
80. J.I. Korenbrot, R.A. a, and Cone, "Dark Ionic Flux and the Effects of Light in Isolated Rod Outer Segments," J. Gen. Physiol. **60**(1), 20–45 (1972).
81. M. Sokolov, A. L. Lyubarsky, K. J. Strissel, *et al.*, "Massive Light-Driven Translocation of Transducin between the Two Major Compartments of Rod Cells: A Novel Mechanism of Light Adaptation," Neuron **34**(1), 95–106 (2002).
82. C. W. Cowan, R. N. Fariss, I. Sokal, *et al.*, "High expression levels in cones of RGS9, the predominant GTPase accelerating protein of rods," Proc. Natl. Acad. Sci. **95**(9), 5351–5356 (1998).
83. X. Zhang, T. G. Wensel, and T. W. Kraft, "GTPase Regulators and Photoresponses in Cones of the Eastern Chipmunk," J. Neurosci. **23**(4), 1287–1297 (2003).
84. M. Michaelides, Z. Li, N. A. Rana, *et al.*, "Novel Mutations and Electrophysiologic Findings in RGS9- and R9AP-Associated Retinal Dysfunction (Bradyopsia)," Ophthalmology **117**(1), 120–127.e1 (2010).
85. K. M. Nishiguchi, M. A. Sandberg, A. C. Kooijman, *et al.*, "Defects in RGS9 or its anchor protein R9AP in patients with slow photoreceptor deactivation," Nature **427**(6969), 75–78 (2004).
86. V. Y. Arshavsky and T. G. Wensel, "Timing Is Everything: GTPase Regulation in Phototransduction," Invest. Ophthalmol. Visual Sci. **54**(12), 7725–7733 (2013).
87. U. Chawla, S. M. D. C. Perera, S. D. E. Fried, *et al.*, "Activation of the G-Protein-Coupled Receptor Rhodopsin by Water," Angew. Chem. Int. Ed. **60**(5), 2288–2295 (2021).
88. R. Sharma, C. Schwarz, D. R. Williams, *et al.*, "In Vivo Two-Photon Fluorescence Kinetics of Primate Rods and Cones," Invest. Ophthalmol. Visual Sci. **57**(2), 647–657 (2016).
89. R. Sharma, C. Schwarz, J. J. Hunter, *et al.*, "Formation and Clearance of All-Trans-Retinol in Rods Investigated in the Living Primate Eye With Two-Photon Ophthalmoscopy," Invest. Ophthalmol. Visual Sci. **58**(1), 604–613 (2017).
90. M. Pöge, J. Mahamid, S. S. Imanishi, *et al.*, "Determinants shaping the nanoscale architecture of the mouse rod outer segment," eLife **10**, e72817 (2021).
91. Y. Ma, R. Dong, T. Song, *et al.*, "Evaluating the effects of three anesthetic regimens on retinal structure and function in the living mouse eye using a customized bimodal OCT/ORG system," J. Phys. D: Appl. Phys. **58**(3), 035401 (2025).
92. S. Tomczewski, P. Węgrzyn, D. Borycki, *et al.*, "Light-adapted flicker optoretinograms captured with a spatio-temporal optical coherence-tomography (STOC-T) system," Biomed. Opt. Express **13**(4), 2186–2201 (2022).
93. Z. Gong, Y. Shi, J. Liu, *et al.*, "Light-adapted flicker-optoretinography based on raster-scan optical coherence tomography towards clinical translation," Biomed. Opt. Express **15**(10), 6036–6051 (2024).
94. B. Tan, E. Mason, B. MacLellan, *et al.*, "Correlation of Visually Evoked Functional and Blood Flow Changes in the Rat Retina Measured With a Combined OCT + ERG System," Invest. Ophthalmol. Visual Sci. **58**(3), 1673–1681 (2017).
95. B. Oakley, "2nd, Potassium and the photoreceptor-dependent pigment epithelial hyperpolarization," J. Gen. Physiol. **70**(4), 405–425 (1977).
96. O. Strauss, "The Retinal Pigment Epithelium in Visual Function," Physiol. Rev. **85**(3), 845–881 (2005).

97. J. R. Sparrrow, D. Hicks, and C. P. Hamel, “The retinal pigment epithelium in health and disease,” Curr. Mol. Med. **10**(9), 802–823 (2010).
98. S. Bialek and S. S. Miller, “K+ and Cl- transport mechanisms in bovine pigment epithelium that could modulate subretinal space volume and composition,” J. Physiol. **475**(3), 401 (1994).
99. J.-D. Li, V. I. Govardovskii, and R. H. Steinberg, “Light-dependent hydration of the space surrounding photoreceptors in the cat retina,” Vis. Neurosci. **11**(4), 743–752 (1994).
100. C. Pfäffle, H. Spahr, L. Kutzner, *et al.*, “Simultaneous functional imaging of neuronal and photoreceptor layers in living human retina,” Opt. Lett. **44**(23), 5671–5674 (2019).
101. C. Pfäffle, H. Spahr, K. Gercke, *et al.*, “Phase-sensitive measurements of depth dependent signal transduction in the inner plexiform layer,” in *Ophthalmic Technologies XXXI*. 2021. SPIE.
102. T. Euler, S. Haverkamp, T. Schubert, *et al.*, “Retinal bipolar cells: elementary building blocks of vision,” Nat. Rev. Neurosci. **15**(8), 507–519 (2014).
103. S. Mozaffari, F. Feroldi, F. LaRocca, *et al.*, “Retinal imaging using adaptive optics optical coherence tomography with fast and accurate real-time tracking,” Biomed. Opt. Express **13**(11), 5909–5925 (2022).
104. J. H. Wong, S. Luo, Z. Hosseinaee, *et al.*, “Optoretinography with actively stabilized adaptive optics optical coherence tomography,” Biomed. Opt. Express **16**(8), 3222–3236 (2025).
105. J. Fong, H. K. Doyle, C. Wang, *et al.*, “Novel color via stimulation of individual photoreceptors at population scale,” Sci. Adv. **11**(16), eadu1052 (2025).
106. H. Spahr, C. Pfäffle, S. Burhan, *et al.*, “Phase-sensitive interferometry of decorrelated speckle patterns,” Sci. Rep. **9**(1), 11748 (2019).
107. K. V. Vienola, D. Valente, R. J. Zawadzki, *et al.*, “Velocity-based optoretinography for clinical applications,” Optica **9**(10), 1100–1108 (2022).
108. M. Hollins and M. Alpern, “Alpern Dark Adaptation and Visual Pigment Regeneration in Human Cones,” J. Gen. Physiol. **62**(4), 430–447 (1973).
109. S. A. Burns, A. E. Elsner, L. A. Lobes, *et al.*, “A psychophysical technique for measuring cone photopigment bleaching,” Invest. Ophthalmol. Visual Sci. **28**(4), 711–717 (1987).
110. S. K. Shevell, “Saturation in human cones,” Vision Res. **17**(3), 427–434 (1977).
111. V. C. Smith, J. Pokorny, and D. Van Norren, “Densitometric measurement of human cone photopigment kinetics,” Vision Res. **23**(5), 517–524 (1983).
112. W. A. H. Rushton and G. H. Henry, “Bleaching and regeneration of cone pigments in man,” Vision Res. **8**(6), 617–631 (1968).
113. S. A. Burns and A. E. Elsner, “Color matching at high illuminances: the color-match-area effect and photopigment bleaching,” J. Opt. Soc. Am. A **2**(5), 698–704 (1985).
114. J. M. Enoch and G. M. Hope, “Directional Sensitivity of the Foveal and Parafoveal Retina,” Invest. Ophthalmol. Visual Sci. **12**(7), 497–503 (1973).
115. C. A. Curcio, K. R. Sloan, R. E. Kalina, *et al.*, “Human photoreceptor topography,” J. Comp. Neurol. **292**(4), 497–523 (1990).
116. X. Jiang, T. Liu, V. P. Pandiyan, *et al.*, “Coarse-scale optoretinography (CoORG) with extended field-of-view for normative characterization,” Biomed. Opt. Express **13**(11), 5989–6002 (2022).
117. R. S. Jonnal, “Toward a clinical optoretinogram: a review of noninvasive, optical tests of retinal neural function,” Ann. Transl. Med. **9**(15), 1270 (2021).
118. M. Gaffney, T.B. Connor, and R.F. Cooper, “Intensity-based optoretinography reveals sub-clinical deficits in cone function in retinitis pigmentosa,” Front. Ophthalmol. **4**, 1373549 (2024).
119. N. Wongchaisuwat, A. Amato, P. Yang, *et al.*, “Optical Coherence Tomography Split-Spectrum Amplitude-Decorrelation Optoretinography Detects Early Central Cone Photoreceptor Dysfunction in Retinal Dystrophies,” *Transl. Vis. Sci. Technol.* 13(10), 5–5 (2024).
120. P. Xu, R. F. Cooper, Y. Y. Jiang, *et al.*, “Parafoveal cone function in choroideremia assessed with adaptive optics optoretinography,” Sci. Rep. **14**(1), 8339 (2024).
121. T. Liu, B. J. Wendel, J. Huey, *et al.*, “Longitudinal Changes in Optoretinography Provide an Early and Sensitive Biomarker of Outer Retinal Disease,” Am. J. Ophthalmol. **277**, 375–386 (2025).
122. G. Ma, T.-H. Kim, T. Son, *et al.*, “Intrinsic signal optoretinography revealing AD-induced retinal photoreceptor hyperexcitability before a detectable morphological abnormality,” Opt. Lett. **48**(19), 5129–5132 (2023).
123. T.-H. Kim, J. Ding, and X. Yao, “Intrinsic signal optoretinography of dark adaptation kinetics,” Sci. Rep. **12**(1), 2475 (2022).